Visualizing the metazoan proliferation-terminal differentiation decision *in vivo*

Abraham Q. Kohrman,[1,7] Rebecca C. Adikes,[1,7] Michael A. Q. Martinez,[1] Nicholas J. Palmisano,[1] Jayson J. Smith,[1] Taylor N. Medwig-Kinney,[1] Mingwei Min,[2] Maria D. Sallee,[3] Ononnah B. Ahmed,[1] Nuri Kim,[1] Simeiyun Liu,[1,4] Robert D. Morabito,[1] Nicholas Weeks,[1] Qinyun Zhao,[1] Wan Zhang,[1] Jessica L. Feldman,[3] Michalis Barkoulas,[5] Ariel M. Pani,[6] Sabrina L. Spencer,[2] Benjamin L. Martin,[1] and David Q. Matus[1,8,*]

[1]Department of Biochemistry and Cell Biology, Stony Brook University, Stony Brook, NY 11794, USA
[2]Department of Biochemistry and BioFrontiers Institute, University of Colorado Boulder, Boulder, CO 80303, USA.
[3]Department of Biology, Stanford University, Stanford, CA 94305, USA.
[4]Current address: Molecular, Cell and Developmental Biology, University of California Santa Cruz, Santa Cruz, CA 95064, USA
[5]Department of Life Sciences, Imperial College, London SW7 2AZ, UK.
[6]Department of Biology, University of Virginia, Charlottesville, VA 22903, USA.
[7]These authors contributed equally
[8]Lead Contact
*Correspondence: david.matus@stonybrook.edu

SUMMARY

Cell proliferation and terminal differentiation are intimately coordinated during metazoan development. Here, we adapt a cyclin-dependent kinase (CDK) sensor to uncouple these cell cycle-associated events live in *C. elegans* and zebrafish. The CDK sensor consists of a fluorescently tagged CDK substrate that steadily translocates from the nucleus to the cytoplasm in response to increasing CDK activity and consequent sensor phosphorylation. We show that the CDK sensor can distinguish cycling cells in G_1 from terminally differentiated cells in G_0, revealing a commitment point and a cryptic stochasticity in an otherwise invariant *C. elegans* cell lineage. We also derive a predictive model of future proliferation behavior in *C. elegans* and zebrafish based on a snapshot of CDK activity in newly born cells. Thus, we introduce a live-cell imaging tool to facilitate *in vivo* studies of cell cycle control in a wide-range of developmental contexts.

KEYWORDS

cell cycle, proliferation, terminal differentiation, CDK sensor, *C. elegans*, Zebrafish, G_1/G_0

INTRODUCTION

Organismal development requires a delicate balance between cell proliferation and cell cycle arrest. In early embryos, the emphasis is placed on rapid cell proliferation, which is achieved by omitting gap phases (G_1 and G_2) and establishing a biphasic cell cycle that rapidly alternates between DNA synthesis (S phase) and mitosis (M phase) (Edgar and O'Farrell, 1989; Newport and Kirschner, 1982). After several rounds of embryonic cell division, the gap phases are introduced, coincident in many organisms with cell fate decisions and the execution of morphogenetic cell behaviors (Foe, 1989; Grosshans and Wieschaus, 2000). These gap phases are believed to function as commitment points for cell cycle progression decisions. The earliest point of commitment occurs during G_1, which is the focus of this study. Cells either engage in cell cycle progression and enter S phase, or they exit the cell cycle altogether and enter a cell cycle arrested state referred to as G_0 and undergo quiescence or terminal differentiation (Sun and Buttitta, 2017). Although the location of the G_1 commitment point in yeast (Start) and cultured mammalian cells (Restriction Point) has in large part been spatiotemporally mapped and molecularly characterized (Hartwell et al., 1974; Pardee, 1974; Spencer et al., 2013), when metazoan cells make this decision *in vivo* while integrating intrinsic and the extrinsic cues of their local microenvironment during development remains poorly understood. A cell cycle sensor that is amenable to such *in vivo* studies can shed new light on this four-decade-old biological phenomenon.

In 2008, Sakaue-Sawano and colleagues engineered a multicolor fluorescent ubiquitination-based cell cycle indicator (FUCCI) for mammalian cell culture (Sakaue-Sawano et al., 2008). FUCCI has since been adapted for many research organisms (Ozpolat et al., 2017; Zielke and Edgar, 2015). However, FUCCI on its own cannot distinguish between a cell residing in G_1 that will cycle again upon completing mitosis and a cell that is poised to enter G_0 (Oki et al., 2014). Separating G_1 from G_0 is essential to understanding mechanisms controlling cell cycle exit during quiescence or terminal differentiation. To distinguish G_1 from G_0 in mammalian cell culture, Hanh, Spencer and colleagues developed and implemented a single-color ratiometric sensor of cell cycle state comprised of a fragment of human DNA helicase B (DHB) fused to a fluorescent protein that is phosphorylated by CDKs (Hahn et al., 2009; Schwarz et al., 2018; Spencer et al., 2013). Notably, through quantitative measurements of CDK activity, this sensor provided new insights into the proliferation-quiescence decision in cultured mammalian cells by identifying cycling cells that exit mitosis in a CDK-increasing (CDK^{inc}) state and quiescent cells that exit

80 mitosis in a CDK-low (CDK^{low}) state (Spencer et al., 2013). Nonetheless, a DHB-based CDK
81 sensor has not been utilized to evaluate the proliferation-terminal differentiation decision.
82
83 In this study, we investigate the proliferation-terminal differentiation decision in *C. elegans*
84 and zebrafish, two powerful *in vivo* systems with radically different modes of development. We
85 generate transgenic CDK sensor lines in each organism to examine this decision live at mitotic
86 exit. By quantifying CDK activity, or DHB ratios, at mitotic exit, we are able to predict future cell
87 behavior across several embryonic and post-embryonic lineages. Despite cells generally exiting
88 mitosis with decreased CDK activity levels, we reliably distinguish cycling cells that exit mitosis
89 into G_1, in a CDK^{inc} state, from terminally differentiated cells that exit mitosis into G_0, in a CDK^{low}
90 state. To gain insights into cell cycle progression commitment, we examine the activity of *C.*
91 *elegans cki-1*, a cyclin-dependent kinase inhibitor (CKI) of the Cip/Kip family, demonstrating that
92 endogenous CKI-1 levels are anti-correlated with CDK activity during the proliferation-terminal
93 differentiation decision. We propose that integration of CKI-1 levels in the mother cell and the high
94 CKI-1/low CDK activity at mitotic exit mediate this decision. By utilizing the CDK sensor to predict
95 future cell behavior, we uncover a cryptic stochasticity that occurs in a temperature-dependent
96 fashion in the *C. elegans* vulva, an otherwise invariant and well-characterized lineage. Finally, we
97 reveal cell cycle dynamics in zebrafish, an organism that lacks a defined cell lineage,
98 demonstrating that differentiated embryonic tissues display DHB ratios that correlate with those
99 observed in terminally differentiated G_0 cells in *C. elegans*. Together, we present a tool for
100 visualizing G_1/G_0 dynamics *in vivo* during metazoan development that can be used to study the
101 interplay between cell proliferation and terminal differentiation.
102
103 **RESULTS**
104
105 **Design and Characterization of a Live *C. elegans* CDK Sensor to Define Interphase States**
106 We synthesized a codon-optimized fragment of human DHB comprised of amino acids 994–1087
107 (Hahn et al., 2009; Spencer et al., 2013). The fragment contains four serine sites that are
108 phosphorylated by CDKs in human cells (Moser et al., 2018; Spencer et al., 2013). These serine
109 sites flank a nuclear localization signal (NLS) situated next to a nuclear export signal (NES)
110 (**Figure 1A**). When CDK activity is low, the NLS is dominant over the NES and DHB localizes to
111 the nucleus. However, when CDK activity increases (i.e., during cell cycle entry), the NLS is
112 obstructed and DHB localizes to the cytoplasm (**Figure 1B**). Using this DHB fragment, we
113 generated two CDK sensors by fusing green fluorescent protein (GFP) or two copies of a red
114 fluorescent protein, mKate2 (2xmKate2), to the DHB C-terminus (**Figure 1A**). To visualize the

115 nucleus, we co-expressed *his-58*/histone H2B fused to 2xmKate2 or GFP, respectively, which is
116 separated from DHB by a P2A self-cleaving viral peptide (Ahier and Jarriault, 2014). We drove
117 the expression of each CDK sensor via a ubiquitous *rps-27* promoter (Ruijtenberg and van den
118 Heuvel, 2015).
119
120 To test both the GFP (**Figure 1C, 1D, S1A**) and 2xmKate2 (**Figure S1B-D)** versions of
121 our CDK sensor, we began by examining cell divisions in the *C. elegans* embryo and germline
122 (**Movie S1**). First, we visualized cells in the embryonic intestine, which is clonally derived from the
123 E blastomere, as these are the first cells in the embryo to have gap phases (Edgar and McGhee,
124 1988). The E blastomere goes through four rounds of divisions to give rise to 16 descendants
125 (E16 cells) about four hours after first cleavage. While 12 of the E16 cells have completed their
126 embryonic divisions at this stage (Leung et al., 1999), four cells called E16* star cells divide once
127 more to generate the 20-celled intestine (E20). Although all E16 cells polarize and show signs of
128 differentiation, the E16* star cells quickly reenter the cell cycle to divide again (Rasmussen et al.,
129 2013; Yang and Feldman, 2015). Thus, we wondered whether our CDK sensor could be used to
130 distinguish between cycling E16* star cells and quiescent E16 cells. To accomplish this, we
131 tracked E16* star cell division from the E16–E20 stage and observed that DHB::GFP localizes in
132 a cell cycle-dependent fashion during these divisions, with DHB::GFP translocating from the
133 nucleus to the cytoplasm and then re-locating to the nucleus at the completion of E16* star cell
134 division (**Figure 1C, S1A**). Consistent with our observations using the GFP version of our CDK
135 sensor in mid-embryogenesis, DHB::2xmKate2 also dynamically translocates from the nucleus to
136 the cytoplasm during cell divisions in the early embryo (**Figure S1B**). Second, we examined the
137 localization of DHB::GFP (**Figure 1D**) and DHB::2xmKate2 (**Figure S1C, S1D**) in the adult *C.*
138 *elegans* germline. Here we detected a gradient of live CDK activity, from high in the distal mitotic
139 progenitor zone to low in the proximal meiotic regions, as described with EdU incorporation and
140 phospho-histone H3 staining (Kocsisova et al., 2018). Together, these results demonstrate that
141 our CDK sensor is dynamic during cell cycle progression in the *C. elegans* embryo and germline.
142
143 The ability to distinguish cycling cells from quiescent cells in the embryo made us wonder
144 whether we could also distinguish cycling cells from terminally differentiated cells post-
145 embryogenesis. Therefore, we examined our CDK sensor in several post-embryonic somatic
146 lineages that undergo proliferation followed by terminal differentiation (Sulston and Horvitz, 1977).
147 Specifically, we selected the sex myoblasts (SM), the somatic sheath (SS) and ventral uterine
148 (VU) cells of the somatic gonad, and the vulval precursor cells (VPCs) (**Figure 1E and E'**). To
149 define each phase of the cell cycle while these lineages are proliferating, we combined static and

150 time-lapse imaging approaches to measure nuclear:cytoplasmic DHB ratios for G_1, S and G_2
151 (**Figure 1F-J, S1E-M**). First, we RNAi depleted the sole *C. elegans* CDK1 homolog, *cdk-1,* to
152 induce a penetrant G_2 phase arrest in the SM cells (**Figure 1F**). Quantification of DHB ratios
153 following *cdk-1* RNAi treatment showed a mean ratio of 1.00±0.28 and 2.36±0.70 in the GFP and
154 2xmKate2 versions of our CDK sensor, respectively (**Figure 1H**). Next, we quantified DHB ratios
155 following time-lapse of SM (**Figure 1F', 1H, S1G**), uterine (**Figure S1E, S1G**) and VPC (**Figure**
156 **S1F, S1G**) divisions to determine peak values of G_2 CDK activity (**Figure 1I, S1H, S1I**). All
157 lineages exhibited the same CDK sensor localization pattern during peak G_2—that is, maximal
158 nuclear exclusion. Next, for each lineage (**Figure 1F'', S1E', S1F'**), we quantified DHB ratios 20
159 minutes after anaphase from our time-lapses to determine a threshold for G1 phase CDK activity.
160 In G1, DHB::GFP and DHB::2xmKate2 were nuclear localized after mitotic exit with mean ratios
161 of 0.59±0.11 and 0.97±0.20 in SMs, 0.67±0.10 and 1.13±0.17 in uterine cells, and 0.35±0.14 and
162 0.58±0.32 in VPCs (**Figure 1H, 1I, S1G-I**). Finally, we paired DHB::2xmKate2 with a reporter for
163 S phase, fusing GFP to the sole *C. elegans* proliferating cell nuclear antigen (PCNA)
164 homolog, *pcn-1*, expressed under its own endogenous promoter at single copy. Although nuclear
165 localized throughout the cell cycle, PCNA forms sub-nuclear puncta solely in S (Brauchle et al.,
166 2003; Dwivedi et al., 2019; Strzyz et al., 2015; Zerjatke et al., 2017). Analysis of time-lapse data
167 found that punctate expression of PCN-1::GFP correlated with mean DHB::2xmKate2 ratios of
168 0.89±0.16 in SM (**Figure 1G, 1J, Movie S2**), 1.00±0.10 in uterine (**Figure S1J, S1K**) and
169 1.02±0.22 in VPC (**Figure S1J, S1K**) lineages. Despite individual lineages showing differences
170 in CDK activity (**Figure S1G**), primarily in G_1, we can establish DHB ratios for each interphase
171 state (G_1/S/G_2) across several post-embryonic somatic lineages using either CDK sensor and
172 recommend pairing with a PCNA reporter for precise determination of interphase state
173 boundaries. We next wondered if we could distinguish G_1 from G_0 as these somatic lineages exit
174 their final cell division; therefore, allowing us to visibly and quantitatively detect terminal
175 differentiation *in vivo*. We mainly chose the DHB::GFP version of our CDK sensor to conduct the
176 following experiments as it was more photostable.
177
178 **CDK^{low} Activity after Mitotic Exit is Predictive of Terminal Differentiation**
179 In asynchronously dividing MCF10A epithelial cell lines, cells that exited mitosis into a $CDK2^{low}$
180 state had a high probability of staying in G_0 compared to cells that exited at a $CDK2^{inc}$ state
181 (Spencer et al., 2013). We therefore wanted to determine whether the cytoplasmic:nuclear ratio
182 of DHB::GFP following an *in vivo* cell division could be used to predict if a cell will enter G_1 and
183 divide again or enter G_0 and terminally differentiate. Taking advantage of the predictable cell

184 lineage pattern of *C. elegans*, we quantitatively correlated DHB::GFP ratios with the decision to
185 proliferate or terminally differentiate. We first quantified DHB::GFP ratios from time-lapse
186 acquisitions of SM cell divisions. The SM cells undergo three rounds of cell division during the L3
187 and L4 larval stages before terminally differentiating into uterine and vulval muscle (**Figure 2A**)
188 (Sulston and Horvitz, 1977). Quantification of DHB::GFP in this lineage revealed that shortly after
189 the first and second divisions, CDK activity increases immediately after mitotic exit from an
190 intermediate level, which we designate as a CDK^{inc} state (**Figure 2B, 2C, Movie S3**), Conversely,
191 CDK activity following the third and terminal division remains low, designated as a CDK^{low} state.
192 Bootstrap analyses support a significant difference in DHB::GFP ratios between pre-terminal
193 (CDK^{inc}) and terminal divisions, but not among pre-terminal divisions (**Figure S2A-C**). We then
194 quantified DHB::GFP ratios during the division of two somatic gonad lineages, the VU and SS
195 cells. They both undergo several rounds of division during the L3 larval stage and terminally
196 differentiate in the early L4 stage (**Figure 2D**) (Sulston and Horvitz, 1977). We quantified a pre-
197 terminal division and the subsequent division that leads to terminal differentiation. Similar to the
198 SM lineage, both somatic gonad lineages exit the round of cell division prior to their final division
199 into a CDK^{inc} state and then exit into a CDK^{low} state following their terminal differentiation (**Figure**
200 **2E, 2F, S2D-F, Movie S4**). Bootstrap analyses support a significant difference between
201 DHB::GFP ratios in pre-terminal versus terminal divisions in the developing somatic gonad
202 (**Figure S2D**).
203
204 Next, we sought to determine how the CDK sensor behaves under conditions in which
205 cells are experimentally forced into G_0. To accomplish this, we generated a single copy transgenic
206 line of mTagBFP2-tagged CKI-1, the *C. elegans* homolog of $p21^{Cip1}$/$p27^{Kip1}$, under an inducible
207 heat shock promoter (*hsp*), paired with a *rps-0*>DHB::mKate2 variant of the CDK sensor. Induced
208 expression of CKI-1 is expected to result in G_0 arrest (Hong et al., 1998; Matus et al., 2014; van
209 der Horst et al., 2019). Indeed, in the SM and uterine lineages, induced expression of CKI-1
210 resulted in cells entering a CDK^{low} G_0 state, with mean DHB ratios of 0.10±0.05 and 0.12±0.05,
211 respectively (**Figure 2G**) as compared to control animals that lacked heat shock-induced
212 expression (SM: 0.99±0.82, uterine: 0.71±0.35) or lacked the inducible transgene (SM:
213 0.96±0.77, uterine: 1.00±0.37). Thus, induced G_0 arrest by ectopic expression of CKI-1 is
214 functionally equivalent, by CDK activity levels, to the G_0 arrest that occurs following mitotic exit in
215 an unperturbed cell destined to undergo terminal differentiation.
216
217 We next examined the divisions of the 1˚- and 2˚-fated VPC lineage. The *C. elegans* vulva
218 is derived from three cells (P5.p–P7.p), which undergo three rounds of cell division during the L3

219 and early L4 larval stages (**Figure 3A, 3B**) (Katz et al., 1995; Sternberg and Horvitz, 1986; Sulston
220 and Horvitz, 1977). Rather than giving rise to 24 cells, the two D cells, the innermost
221 granddaughters of the 2˚-fated P5.p and P7.p, terminally differentiate one round of cell division
222 early. This results in a total of 22 cells which comprise the adult vulva (Katz et al., 1995; Sulston
223 and Horvitz, 1977). Quantification of DHB::GFP ratios during VPC divisions yielded the expected
224 pattern. The daughters of P5.p–P7.p all exited their first division into a CDK^{inc} state (**Figure 3C,**
225 **3D).** After the next division, the 12 granddaughters of P5.p–P7.p (named A–F symmetrically) are
226 born, including the terminally differentiated D cell (Katz et al., 1995; Sulston and Horvitz, 1977).
227 At this division, the strong nuclear localization of DHB::GFP in the D cell was in stark contrast to
228 the remaining proliferating VPCs. The D cell exited into and remained in a CDK^{low} state, while the
229 remaining VPCs exited into a CDK^{inc} state and continued to progress through the cell cycle
230 (**Figure 3C, 3D, Movie S5**). All remaining VPCs exited into a CDK^{low} state at their terminal
231 division. Consistent with these results, bootstrap analyses (**Figure S2G-M**) support our qualitative
232 results, such that we can quantitatively distinguish between a cell that has completed mitosis and
233 will continue to cycle (CDK^{inc}) from a cell that exits mitosis and enters a terminally differentiated
234 G_0 state (CDK^{low}).
235
236 **CKI-1 Levels Peak Prior to Terminal Differentiation**
237 In mammalian cell culture, endogenous levels of $p21^{Cip1}$ during G_2 are predictive of whether a cell
238 will go on to divide or enter quiescence/senescence/terminal differentiation (Hsu et al., 2019;
239 Moser et al., 2018; Overton et al., 2014; Spencer et al., 2013). This raises the intriguing possibility
240 that endogenous levels of CKI-1 in *C. elegans* correlate with CDK^{low} or CDK^{inc} activity. To co-
241 visualize CKI-1 dynamics with our CDK sensor, we inserted a N-terminal GFP tag into the
242 endogenous locus of *cki-1* via CRISPR/Cas9 and introduced a DHB::2xmKate2 variant of the
243 sensor (devoid of histone H2B) into this genetic background. Since endogenous levels of
244 GFP::CKI-1 were too dim for time-lapse microscopy, likely due to its short half-life (Yang et al.,
245 2017), we collected a developmental time series of static images over the L3 and L4 larval stages
246 to characterize GFP::CKI-1 levels during pre-terminal and terminal divisions in the VPC lineage.
247 We detected generally low levels of GFP::CKI-1 at the Pn.p 2-cell stage (**Figure 4A, 4B, S3A-C**).
248 In their daughter cells, at the Pn.p 4-cell stage, we detected an increase in GFP::CKI-1 levels in
249 cycling cells prior to their next cell division, peaking in G_2 (**Figure 4A, 4C, S3A-C**). Notably, the D
250 cell, which becomes post-mitotic after this cell division, exits mitosis with higher levels of
251 GFP::CKI-1 than its CD mother (**Figure 4A and S3B**). This trend holds true for the remaining
252 VPCs during terminal differentiation at the Pn.p 6-cell and 8-cell stage, which show high levels of

253 GFP::CKI-1 that peak immediately after mitotic exit and remain high during the post-mitotic L4
254 stage (**Figure 4A, 4D, 4E, S4A-C**). We also observed increasing levels of GFP::CKI-1 in the G_2
255 phase of mother cells that peak in their terminal daughter cells in the uterine (**Figure S3D**) and
256 SM cell lineages (**Figure S3E**). Thus, levels of GFP::CKI-1 increase in mother cells prior to
257 terminal differentiation and remain high upon mitotic exit in daughter cells with CDK^{low} activity.
258 These results elucidate a proliferation-terminal differentiation decision process that is already
259 underway in G_2 of the previous cell cycle and is in part controlled by CKI-1 in the mother cell.
260
261 During our collection of static images of GFP::CKI-1 animals, we observed significant
262 deviations in the expected VPC lineage pattern in the early L4 larval stage. In particular, we noted
263 that many cells appeared to bypass their final division and undergo early terminal differentiation
264 with coincident high levels of GFP::CKI-1 and low DHB ratios. We hypothesized that the line we
265 generated could be behaving as a gain-of-function mutant, as GFP insertions at the N-terminus
266 could interfere with proteasome-mediated protein degradation of CKI-1 (Bloom et al., 2003). The
267 penetrance of this early terminal differentiation defect varied across VPC lineages. While the A
268 (2% of cases observed) and E (3% of cases observed) lineages showed a low penetrance of this
269 early terminal differentiation defect, the B (26% of cases observed) and F (58% of cases
270 observed) lineages showed a moderate penetrance (**Figure 4F, 4G**). We speculate that the A
271 and E lineages are largely insensitive to the gain-of-function mutant because CKI-2, an
272 understudied paralog of CKI-1, is the dominant CKI in these cells. The C cell, sister to the
273 terminally differentiated D cell, had a highly penetrant early terminal differentiation defect (98% of
274 cases observed; **Figure 4F, 4G**). Consistent with our finding that high levels of endogenous
275 GFP::CKI-1 can lead to early terminal differentiation, heat shock-induced CKI-1 expression
276 uniformly drove VPCs into a CDK^{low} G_0 state with mean DHB ratios of 0.11±0.05 (**Figure 4H**) as
277 compared to control animals that lacked heat shock-induced expression (0.46±0.87) or lacked the
278 inducible *cki-1* transgene (0.47±0.42). Together, these results demonstrate that cycling cells are
279 highly sensitive to levels of CKIs and that increased expression can induce a terminally
280 differentiated G_0 state.
281
282 **CDK Activity Predicts a Cryptic Stochastic Fate Decision in an Invariant Cell Lineage**
283 A strength of *C. elegans* is the organism's robust ability to buffer external and internal
284 perturbations to maintain its invariant cell lineage. However, not all cell divisions that give rise to
285 the 959 somatic cells are completely invariant. Studies have identified several lineages, including
286 the vulva, in *C. elegans* where environmental stressors, genetic mutations and/or genetic
287 divergence of wild isolates leads to stochastic changes in a highly invariant cell fate pattern

288 (Braendle and Felix, 2008; Hintze et al., 2020; Katsanos et al., 2017). Thus, we wondered if the
289 CDK sensor generated here could be utilized to visualize and predict stochastic lineage decisions
290 during *C. elegans* development.
291
292 The VPC lineage that gives rise to the adult vulva is invariant (**Figure 5A, S4A**) (Sulston
293 and Horvitz, 1977). However, at high temperatures it has been observed that the D cell, the inner-
294 most granddaughter of P5.p or P7.p, will go on to divide (**Figure 5A**) (Sternberg, 1984; Sternberg
295 and Horvitz, 1986). Unexpectedly, we noticed a rare occurrence of D cells expressing elevated
296 DHB ratios during the course of time-lapse analysis of VPC divisions captured under standard
297 laboratory conditions. To determine the penetrance of the cycling D cell phenotype, we inspected
298 each of our CDK sensor lines grown at 25°C, a high temperature that is still within normal range
299 for *C. elegans*. In both strains we observed a cycling D cell with a 2-10% penetrance (**Figure 5B,**
300 **S4B**). To test whether this cycling D cell phenotype resulted from the presence of the DHB
301 transgene or environmental stressors, such as temperature fluctuation, we examined the VPC
302 lineage in animals lacking the CDK sensor at 25°C and 28°C. At 25°C, we observed a low
303 penetrance (2%) of cycling D cells in a strain expressing an endogenously tagged DNA licensing
304 factor, CDT-1::GFP (**Figure 5B, S4B**), which is cytosolic in cycling cells (Matus et al., 2014;
305 Matus et al., 2015). From lineage analysis, L2 larvae, expressing a seam cell reporter (*scm*>GFP),
306 that were temperature shifted from 20°C to 28°C displayed approximately a 30% occurrence of
307 extra D cell divisions (**Figure S4C-E**). Lastly, we wanted to determine whether D cells that show
308 CDK^{inc} activity divide. To accomplish this, we collected time-lapses of DHB::GFP animals grown
309 at 25°C. These time-lapses revealed 10 occurrences of D cells born into a CDK^{inc} rather than a
310 CDK^{low} (**Figure 5C, 5D, Movie S6**). In all 10 cases, the CDK^{inc} D cell goes on to divide (**Figure**
311 **S4A**). Thus, we find that CDK activity shortly after mitosis is a strong predictor of future cell
312 behavior, even in rare stochastic cases of extra cell divisions in *C. elegans*, an organism with a
313 well-defined cell lineage.
314
315 **Generation of Inducible CDK Sensor Transgenic Lines in Zebrafish**
316 To investigate the predictive capability of DHB ratios in zebrafish, we generated two CDK sensor
317 lines with different fluorescent protein combinations, DHB-mNeonGreen (mNG) and DHB-
318 mScarlet (DHB-mSc) with H2B-mSc and H2B-miRFP670, respectively, to allow for flexibility with
319 imaging and experimental design (**Figure 6A**). Both transgenes are under the control of the
320 *hsp70l* heat shock-inducible promoter, which produces robust ubiquitous expression after shifting
321 the temperature from 28.5˚C to 40˚C for 30 minutes (Halloran et al., 2000; Shoji et al., 1998). We
322 also generated a transgenic line, *Tg(ubb:Lck-mNG)*, that ubiquitously labels the plasma

membrane with mNG, which we crossed into the HS:DHB-mSc-2A-H2B-miRFP670 line to simultaneously visualize CDK activity (DHB-mSc), segment nuclei (H2B-miRFP670) and segment the plasma membrane (LCK-mNG) (**Figure 6A**).

To verify that both CDK sensor lines localize DHB in a cell cycle-dependent manner, we first used time-lapse microscopy and quantified DHB ratios across cell divisions in the tailbud of bud or 22 somite-stage embryos to determine peak G_2 and G_1 DHB ratios (**Figure 6B-D**). We observed the expected localization pattern for both CDK sensor lines, with maximal nuclear exclusion of the sensor shortly before mitosis in G2 (3.42±0.56 and 6.57±2.00) and low DHB ratios (0.69±0.17 (mNG) and 0.51±0.21 (mSC)) representing nuclear accumulation of the sensor shortly after mitosis in G1 (**Figure 6C, 6D**). Thus, we conclude that both CDK sensor lines localize in a cell cycle-dependent fashion, and that quantitative measurements can be used to determine interphase states.

Next, using both DHB transgenic lines, we examined CDK activity in a number of defined embryonic tissues. Imaging of the developing tailbud reveled cells in all phases of the cell cycle with a mean DHB ratios of 1.95±1.74 (mNG) and 1.67±2.05 (mSC) (**Figure 6E, 6F)**. The tailbud of vertebrate embryos contain neuromesodermal progenitors (NMPs) (Martin, 2016), which in zebrafish have been reported to be predominantly arrested in the G_2 phase of the cell cycle (Bouldin et al., 2014). Consistent with this, we observed cells with high CDK activity in the tailbud (**Figure 6E, S5A** orange arrows). This enrichment is eliminated when embryos are treated with the CDK4/6 inhibitor palbociclib, leading to a significant increase of cells in the tailbud with low CDK activity (0.58±0.31), similar in range to the G_1/G_0 values we measured during time-lapse (0.69±0.17) (**Figure S5D-F**). Finally, we made the surprising observation that primitive red blood cells in the intermediate cell mass of 24 hours post-fertilization (hpf) embryos, which are nucleated in zebrafish, display high CDK activity (3.00±0.97) indicating that they are exclusively in the G_2 phase of the cell cycle (**Figure S5B**), suggesting that cell cycle regulation may be important for hematopoiesis (Bronnimann et al., 2018; De La Garza et al., 2019)

Visualization of Proliferation and Terminal Differentiation during Zebrafish Development

To examine differences between proliferating and terminally differentiated cells, we examined CDK activity in the somites, which are segmental mesodermal structures that give rise to terminally differentiated skeletal muscle cells and other cell types (Martin, 2016). In the most recently formed somites at 24 hpf, cells can be observed in all phases of the cell cycle (**Figure 6G, 6H**). Consistent with what we observed in the NMPs in the tailbud, treatment with palbociclib

358 also caused somite cells to arrest with low CDK activity (0.33±0.42) in G_1/G_0 (**Figure S5D-F**).
359 Recently formed somites contain a subpopulation of cells called adaxial cells, which are
360 positioned at the medial edge of the somite next to the axial mesoderm. These are the slow
361 muscle precursors and are considered to be in a terminally differentiated state through the
362 cooperative action of Cdkn1ca (p57) and Myod (Osborn et al., 2011). As opposed to the majority
363 of cells in the lateral regions of recently formed somites, adaxial cells possess low CDK activity
364 (0.13±0.04 (mNG)) (**Figure S5C**). At later stages, the majority of cells in the lateral regions of the
365 somite will differentiate into fast skeletal muscles fibers, which are also considered to be in a
366 terminally differentiated state (Halevy et al., 1995). Examination of DHB ratios at 72 hpf skeletal
367 muscle fibers revealed they have low CDK activity (0.14±0.04 (mNG) and 0.13±0.04 (mSc)),
368 similar to the adaxial cells, but significantly different than the mean DHB ratios of undifferentiated
369 cells at 24 hours (0.82±0.70 (mNG) and 0.99±0.084 (mSc)) (**Figure 6A, 6C**). Thus, from our static
370 imaging, we can identify cell types with low CDK activity that are thought to be terminally
371 differentiated.
372
373 We next sought to determine if we can differentiate between the G_1 and G_0 state based
374 on ratiometric quantification of DHB. We compared the terminally differentiated muscle and
375 epidermal cells to notochord progenitor cells, which are held transiently in G_1/G_0 before re-
376 entering the cell cycle upon joining the notochord (Sugiyama et al., 2014; Sugiyama et al., 2009)
377 (**Figure 6I**). Notably, the mean DHB-mNG ratio of the notochord progenitors (0.32±0.08) is
378 significantly higher than the DHB-mNG ratio of the differentiated epidermis (0.13±0.03) (**Figure**
379 **6J**). This value is consistent in notochord progenitors at two other earlier developmental stages,
380 90% epiboly (0.28±0.08) and 18 somites (0.27±0.09) (**Figure 6J**)**.** The DHB-mSc ratio in the
381 notochord progenitors (0.33±0.08) is also significantly different than the differentiated epidermis
382 (0.09±0.04) (**Figure 6J**). Based on this difference in DHB ratios between notochord progenitors
383 and terminally differentiated cell types, including muscle (**Figure 6H**) and epidermis (**Figure 6J**),
384 and our knowledge of the normal biology of these cells, we conclude that the CDK sensor can
385 distinguish between a cycling G_1 state and a terminally differentiated G_0 state in the zebrafish.
386
387 **A Bifurcation in CDK Activity at Mitosis is Conserved in *C. elegans* and Zebrafish**
388 We next investigated whether zebrafish cells separate into G_1/CDK^{inc} and G_0/CDK^{low} populations
389 as they do in the nematode *C. elegans* and whether these CDK activity states are a general
390 predictor of future cell behavior in both animals. First, we plotted all of the time-lapse CDK sensor
391 data we collected in *C. elegans* (**Figure 7A, 7B**) and zebrafish (**Figure 7C, 7D**). For *C. elegans*,
392 plotting of all CDK sensor trace data, irrespective of lineage, demonstrated that cells entering a

393 CDK^{low} state after mitosis corresponded to terminally differentiated cells, while cells that exited
394 mitosis into a CDK^{inc} state corresponded to cells from pre-terminal divisions. For zebrafish, in a
395 lineage agnostic manner, we plotted all the traces from the tailbud and found that these data could
396 also be classified into CDK^{low} and CDK^{inc} populations.
397
398 As we were able to detect a rare stochastic lineage change in the *C. elegans* vulval lineage
399 (**Figure 5**), we selected all CDK sensor trace data from the *C. elegans* VPCs (**Figure S6A**) and
400 used this data to build a classifier to predict pre-terminal (G_1) vs terminal (G_0) cell fates based on
401 CDK activity after anaphase (**Figure S6A-C**). Cross-examining our modeling with the known cell
402 VPC lineage demonstrated that at 20 minutes after anaphase we had 85% accuracy in predictions
403 with near perfect prediction 60 minutes after anaphase (**Figure S6B**). To test the predictive power
404 of the classifier, we analyzed CDK trace data from the births of C and D cells, where some D cells
405 stochastically divide (**Figure 5**). Our classifier correctly predicted cell fate 92% of the time (**Figure**
406 **S6**). Together, these results demonstrate that during development, cycling cells encounter a
407 bifurcation in CDK activity following mitosis where they either: (1) increase in CDK activity and
408 become poised to cycle, or (2) exit into a a CDK^{low} state and undergo terminal differentiation
409 (**Figure 7E**). Thus, we suggest a model where cells from developing tissue in *C. elegans* and
410 zebrafish must cross an early commitment point in the cell cycle where these cells must make the
411 decision to divide or terminally differentiate. The decision to undergo terminal differentiation is
412 crucial to tissue integration and organization and is controlled by the activity of evolutionarily
413 conserved CKI(s) in the mother cell (**Figure 7E**) that control daughter cell CDK activity.
414
415 **DISCUSSION**
416
417 **A CDK Sensor for Live-Cell In Vivo Imaging of Interphase States and the G_1/G_0 Transition**
418 We introduce here a CDK activity sensor to visually monitor interphase and the proliferation-
419 terminal differentiation decision in real-time and *in vivo* in two widely used research organisms,
420 *C. elegans* and zebrafish. This sensor, which reads out the phosphorylation of a DHB peptide by
421 CDKs (Hahn et al., 2009; Spencer et al., 2013), allows for quantitative assessment of cell cycle
422 state, including G_0. The use of FUCCI in zebrafish (Bouldin and Kimelman, 2014; Sugiyama et
423 al., 2009) and past iterations of a CDK sensor in *C. elegans* (Deng et al., 2020; Dwivedi et al.,
424 2019; van Rijnberk et al., 2017) and *Drosophila* (Hur et al., 2020) have been informative in
425 improving our understanding of cell cycle regulation of development, but have not addressed the
426 proliferation-terminal differentiation decision. The DHB transgenic lines generated in this study
427 will allow researchers to distinguish G_1 from G_0 shortly after a cell has divided and directly study

428 G_0-related cell behaviors, such as terminal differentiation, quiescence and senescence, in living
429 organisms.
430
431 CDK sensors have been used previously to visualize the difference between proliferative
432 and quiescent cells in asynchronous mammalian cell culture populations (Arora et al., 2017;
433 Cappell et al., 2016; Gast et al., 2018; Gookin et al., 2017; Miller et al., 2018; Moser et al., 2018;
434 Overton et al., 2014; Spencer et al., 2013; Yang et al., 2015). As mammalian cells complete
435 mitosis, they are born into either a $CDK2^{inc}$ state where they are more likely to divide again, or a
436 $CDK2^{low}$ state where they remain quiescent for longer periods of time. Here we have examined
437 the CDK activity state of cells in an invertebrate with a well-defined and invariant lineage, *C.*
438 *elegans*, and a vertebrate that lacks a defined cell lineage, the zebrafish. In both contexts, we can
439 visually and quantitatively differentiate between cells that are in a CDK^{inc} state following cell
440 division and cells that are in a CDK^{low} state. Strikingly, in *C. elegans* these states precisely
441 correlate with the lineage pattern of the three post-embryonic tissues we examined: the SM cells,
442 uterine cells and VPCs. Cells born into a CDK^{inc} state represented pre-terminal divisions, whereas
443 cells born into a CDK^{low} state were terminally differentiated. By distinguishing these two states in
444 CDK activity, we were able to accurately identify shortly after cell birth a rare stochasticity that
445 was first described through careful end-point lineage analysis nearly 36 years ago in the *C.*
446 *elegans* vulval lineage (Sternberg, 1984; Sternberg and Horvitz, 1986). Further, statistical
447 modeling demonstrated that we could predict future cell behavior with >85% accuracy in *C.*
448 *elegans* just 20 minutes after anaphase and accurately categorized the few cases of stochastic
449 extra cell division we captured during our time-lapse recordings. In zebrafish, we found that we
450 could readily distinguish between CDK^{inc} cells in G_1, such as notochord progenitors which re-enter
451 the cell cycle after joining the notochord, and tissues that are terminally differentiated and contain
452 CDK^{low} cells in G_0, such as skeletal muscle and epidermis. Thus, in both organisms the CDK
453 sensor can be easily used to separate G_1 from G_0 without the need for multiple fluorescent
454 reporters (Bajar et al., 2016; Oki et al., 2014) or fixation and antibody staining for FACS analysis
455 (Tomura et al., 2013).
456
457 **In Vivo Evidence of a G_2 Commitment Point in the Metazoan Cell Cycle**
458 The classic model of the Restriction Point, the point in G_1 at which cells in culture decide to commit
459 to the cell cycle and no longer require growth factors (e.g., mitogens), is that mammalian cells are
460 born uncommitted and that the cell cycle progression decision is not made until several hours
461 after mitosis (Jones and Kazlauskas, 2001; Pardee, 1974; Zetterberg and Larsson, 1985; Zwang
462 et al., 2011). An alternative model has been proposed in studies using single-cell measurements

463 of CDK2 activity in asynchronous populations of MCF10A cells (Spencer et al., 2013) and other
464 nontumorigenic as well as tumorigenic cell lines (Moser et al., 2018). This model extends the
465 classic Restriction Point model for cell cycle commitment. During the G_2 phase of the cell cycle,
466 the mother cell is influenced by levels of p21 and cyclin D and these levels affect the
467 phosphorylation state of Rb in CDK^{low} and CDK^{inc} daughter cells, respectively (Min et al., 2020;
468 Moser et al., 2018). In CDK^{low} daughter cells, phospho-Rb is low and these cells are still sensitive
469 to mitogens. Whether cells *in vivo* coordinate cell cycle commitment with levels of CKI and CDK
470 over this extended Restriction Point is poorly understood.
471
472 By first quantifying the cytoplasmic:nuclear ratio of the CDK sensor in time-lapse
473 recordings of cell divisions in *C. elegans* somatic lineages, we were able to use DHB ratios as a
474 proxy for CDK levels to distinguish two populations of daughter cells: the first being actively cycling
475 cells in a CDK^{inc} state (G_1), and the second being terminally differentiated cells in a CDK^{low} state
476 (G_0). We then quantified cytoplasmic:nuclear ratio of the CDK sensor in time-lapse recordings of
477 cell divisions in zebrafish and were also able to distinguish two populations of daughter cells. As
478 data from asynchronous cell culture studies suggest that the decision to commit to the cell cycle
479 is made by the mother cell as early as G_2 (Moser et al., 2018; Spencer et al., 2013), we wanted
480 to determine if this same phenomenon occurred *in vivo*. To accomplish this, we endogenously
481 tagged one of two CKIs in the *C. elegans* genome, *cki-1*, with GFP using CRISPR/Cas9. We
482 paired static live-cell imaging of GFP::CKI-1 with DHB::2xmKate2 during vulval development.
483 Similar to *in vitro* experiments (Moser et al., 2018; Spencer et al., 2013), we found that mother
484 cells whose daughters are born into a CDK^{inc} G_1 state will divide again, expressing low levels of
485 GFP::CKI-1. In contrast, mother cells of daughters that will differentiate express a peak of
486 GFP::CKI-1 in G_2 which increases as daughter cells are born into a CDK^{low} G_0 state. Thus, our
487 data demonstrate that an extended Restriction Point exists in the cell cycle of intact Metazoa, and
488 that the *in vivo* proliferation-terminal differentiation decision can be predicted in *C. elegans* by
489 CKI/CDK activity shortly after mitotic exit.
490
491 **Conclusion**
492 We demonstrate here that the CDK sensor functions in both *C. elegans* and zebrafish to read out
493 cell cycle state dynamically, and unlike other cell cycle sensors, can distinguish between
494 proliferative and terminally differentiated cells within an hour of cell birth. As nematodes and
495 vertebrates last shared a common ancestor over 500 million years ago, this suggests that the
496 CDK sensor is likely to function in a similar fashion across Metazoa. Thus, this broad functionality
497 will provide a powerful tool to examine fundamental questions such as the relationship between

cell cycle state and cell fate during normal development, cellular reprogramming and tissue regeneration. Finally, as an increasing body of evidence suggests that cell cycle state impinges on morphogenetic events ranging from gastrulation (Grosshans and Wieschaus, 2000; Murakami et al., 2004), convergent extension (Leise and Mueller, 2004) and cellular invasion (Kohrman and Matus, 2017; Matus et al., 2015; Medwig-Kinney et al., 2020), this CDK sensor will provide the means to increase our understanding of the relationship between interphase states and morphogenesis during normal development and diseases arising from cell cycle defects, such as cancer.

SUPPLEMENTAL INFORMATION

Supplemental Information includes Extended Experimental Procedures, six figures, one table, and seven movies, which can be found online with this article.

ACKNOWLEDGEMENTS

We thank D. Özpolat, D. Pisconti, C.-K. Hu and M.J. Gacha-Garay for helpful comments on the manuscript; J. Maghakian and L. Yang for consultation on statistical modeling; D. Dickinson and B. Goldstein for assistance with the CRISPR single copy knock-in strategy; and T. Geer of Nobska Imaging, Inc. for helping maintain our spinning disk confocal microscopes. This work was funded by the NIH NIGMS [1R01GM121597-01 to D.Q.M. and 1R01GM124282 to B.L.M.]. D.Q.M. and B.L.M. are Damon Runyon-Rachleff Innovators supported by the Damon Runyon Cancer Research Foundation [DRR-47-17]. B.L.M. also received support from the NSF [IOS 1452928] and the Pershing Square Sohn Cancer Research Alliance. R.C.A., A.Q.K., J.J.S. and M.A.Q.M. are all supported by the NIGMS [1F32133131-01, F31GM128319-01, 3R01GM121597-02S1/S2, respectively]. T.N.M-K. is supported by the NIH NICHD [F31HD100091-01]. N.J.P. is supported by the ACS [132969-PF-18-226-01-CSM]. J.L.F. and S.L.S. are both supported by an NIH Director's New Innovator Award (DP2GM1191136-01 and DP2-CA238330, respectively). S.L.S. is also supported by an ACS Research Scholar Grant (RSG-18-008-01), a Pew-Stewart Scholar Award, a Beckman Young Investigator Award, a Boettcher Webb-Waring Early-Career Investigator Award, a Kimmel Scholar Award (SKF16-126), and a Searle Scholar Award (SSP-2016-1533). Some strains were provided by the *Caenorhabditis* Genetics Center, which is funded by the NIH ORIP [P40 OD010440].

AUTHOR CONTRIBUTIONS

Conceptualization, R.C.A., A.Q.K., M.A.Q.M., M.D.S., J.L.F., S.L.S., B.L.M. and D.Q.M.; Methodology, R.C.A., A.Q.K., M.A.Q.M., N.J.P., J.J.S., T.N.M-K., S.L., R.D.M., W.Z., B.L.M., and D.Q.M.; Formal Analysis, R.C.A., M.A.Q.M., N.J.P., A.Q.K., T.N.M-K., M.M., S.L.S, B.L.M. and D.Q.M.; Investigation, R.C.A., A.Q.K., M.A.Q.M., N.J.P., J.J.S., M.D.S., O.B.A., N.K., N.W., M.B., A.M.P., B.L.M. and D.Q.M.; Writing, M.A.Q.M, R.C.A., A.Q.K., T.N.M-K., B.L.M and D.Q.M.; Visualization, R.C.A., M.A.Q.M, T.N.M-K. and D.Q.M.; Funding Acquisition, A.Q.K., R.C.A., N.J.P., T.N.M-K., B.L.M. and D.Q.M.

DECLARATION OF INTERESTS

The authors declare no competing interests.

EXPERIMENTAL PROCEDURES

C. elegans Strains

C. elegans strains were cultured in standard conditions at 15-25°C on NGM plates with *E. coli* OP50. In the text and figures, we designate linkage to a promoter with a greater than symbol (>) and use a double colon (::) for linkages that fuse open reading frames (Ziel et al., 2009). See **Extended Experimental Procedures** and the **Key Resources Table** for details about alleles and transgenes generated in this study.

Zebrafish Lines

All zebrafish experiments and husbandry were performed with approval from the Stony Brook University Institutional Animal Care and Use Committee. See **Extended Experimental Procedures** and the **Key Resources Table** for details about the transgenic lines generated used in this study.

RNAi, Heat Shock Induction and Chemical Inhibitors

RNAi was delivered by feeding worms *E. coli* HT115(DE3) expressing double-stranded RNA (dsRNA) targeted against *control* (L4440) and *cdk-1*. Expression of *cki-1* was induced using a ubiquitous heat shock promoter. The inhibitor used in zebrafish was PD-0332991, a CDK4/6 inhibitor. See **Extended Experimental Procedures**.

Live-Cell Microscopy

For microscopes and imaging conditions, see **Extended Experimental Procedures**.

Image Processing and Statistical Analyses

Image processing was performed in Fiji and statistical analyses were performed in MATLAB. See **Extended Experimental Procedures**.

592 **REFERENCES**
593

594 1. Ahier, A., and Jarriault, S. (2014). Simultaneous expression of multiple proteins under a
595 single promoter in Caenorhabditis elegans via a versatile 2A-based toolkit. Genetics *196*, 605-
596 613.
597 2. Arora, M., Moser, J., Phadke, H., Basha, A.A., and Spencer, S.L. (2017). Endogenous
598 Replication Stress in Mother Cells Leads to Quiescence of Daughter Cells. Cell Rep *19*, 1351-
599 1364.
600 3. Bajar, B.T., Lam, A.J., Badiee, R.K., Oh, Y.H., Chu, J., Zhou, X.X., Kim, N., Kim, B.B.,
601 Chung, M., Yablonovitch, A.L.*, et al.* (2016). Fluorescent indicators for simultaneous reporting of
602 all four cell cycle phases. Nat Methods *13*, 993-996.
603 4. Bloom, J., Amador, V., Bartolini, F., DeMartino, G., and Pagano, M. (2003). Proteasome-
604 mediated degradation of p21 via N-terminal ubiquitinylation. Cell *115*, 71-82.
605 5. Bouldin, C.M., and Kimelman, D. (2014). Dual fucci: a new transgenic line for studying
606 the cell cycle from embryos to adults. Zebrafish *11*, 182-183.
607 6. Bouldin, C.M., Snelson, C.D., Farr, G.H., 3rd, and Kimelman, D. (2014). Restricted
608 expression of cdc25a in the tailbud is essential for formation of the zebrafish posterior body.
609 Genes Dev *28*, 384-395.
610 7. Braendle, C., and Felix, M.A. (2008). Plasticity and errors of a robust developmental
611 system in different environments. Dev Cell *15*, 714-724.
612 8. Brauchle, M., Baumer, K., and Gonczy, P. (2003). Differential activation of the DNA
613 replication checkpoint contributes to asynchrony of cell division in C. elegans embryos. Curr Biol
614 *13*, 819-827.
615 9. Bronnimann, D., Annese, T., Gorr, T.A., and Djonov, V. (2018). Splitting of circulating
616 red blood cells as an in vivo mechanism of erythrocyte maturation in developing zebrafish, chick
617 and mouse embryos. J Exp Biol *221*.
618 10. Cappell, S.D., Chung, M., Jaimovich, A., Spencer, S.L., and Meyer, T. (2016).
619 Irreversible APC(Cdh1) Inactivation Underlies the Point of No Return for Cell-Cycle Entry. Cell
620 *166*, 167-180.
621 11. De La Garza, A., Cameron, R.C., Gupta, V., Fraint, E., Nik, S., and Bowman, T.V.
622 (2019). The splicing factor Sf3b1 regulates erythroid maturation and proliferation via TGFbeta
623 signaling in zebrafish. Blood Adv *3*, 2093-2104.
624 12. Deng, T., Stempor, P., Appert, A., Daube, M., Ahringer, J., Hajnal, A., and Lattmann, E.
625 (2020). The Caenorhabditis elegans homolog of the Evi1 proto-oncogene, egl-43, coordinates
626 G1 cell cycle arrest with pro-invasive gene expression during anchor cell invasion. PLoS Genet
627 *16*, e1008470.
628 13. Dwivedi, V.K., Pardo-Pastor, C., Droste, R., Denning, D.P., Rosenblatt, J., and Horvitz,
629 H.R. (2019). Cell cycle S-phase arrest drives cell extrusion. bioRxiv, 839845.
630 14. Edgar, B.A., and O'Farrell, P.H. (1989). Genetic control of cell division patterns in the
631 Drosophila embryo. Cell *57*, 177-187.
632 15. Edgar, L.G., and McGhee, J.D. (1988). DNA synthesis and the control of embryonic
633 gene expression in C. elegans. Cell *53*, 589-599.
634 16. Foe, V.E. (1989). Mitotic domains reveal early commitment of cells in Drosophila
635 embryos. Development *107*, 1-22.
636 17. Gast, C.E., Silk, A.D., Zarour, L., Riegler, L., Burkhart, J.G., Gustafson, K.T., Parappilly,
637 M.S., Roh-Johnson, M., Goodman, J.R., Olson, B.*, et al.* (2018). Cell fusion potentiates tumor
638 heterogeneity and reveals circulating hybrid cells that correlate with stage and survival. Sci Adv
639 *4*, eaat7828.
640 18. Gookin, S., Min, M., Phadke, H., Chung, M., Moser, J., Miller, I., Carter, D., and
641 Spencer, S.L. (2017). A map of protein dynamics during cell-cycle progression and cell-cycle
642 exit. PLoS Biol *15*, e2003268.

643 19. Grosshans, J., and Wieschaus, E. (2000). A genetic link between morphogenesis and
644 cell division during formation of the ventral furrow in Drosophila. Cell *101*, 523-531.
645 20. Hahn, A.T., Jones, J.T., and Meyer, T. (2009). Quantitative analysis of cell cycle phase
646 durations and PC12 differentiation using fluorescent biosensors. Cell Cycle *8*, 1044-1052.
647 21. Halevy, O., Novitch, B.G., Spicer, D.B., Skapek, S.X., Rhee, J., Hannon, G.J., Beach,
648 D., and Lassar, A.B. (1995). Correlation of terminal cell cycle arrest of skeletal muscle with
649 induction of p21 by MyoD. Science *267*, 1018-1021.
650 22. Halloran, M.C., Sato-Maeda, M., Warren, J.T., Su, F., Lele, Z., Krone, P.H., Kuwada,
651 J.Y., and Shoji, W. (2000). Laser-induced gene expression in specific cells of transgenic
652 zebrafish. Development *127*, 1953-1960.
653 23. Hartwell, L.H., Culotti, J., Pringle, J.R., and Reid, B.J. (1974). Genetic control of the cell
654 division cycle in yeast. Science *183*, 46-51.
655 24. Hintze, M., Koneru, S.L., Gilbert, S.P.R., Katsanos, D., Lambert, J., and Barkoulas, M.
656 (2020). A Cell Fate Switch in the Caenorhabditis elegans Seam Cell Lineage Occurs Through
657 Modulation of the Wnt Asymmetry Pathway in Response to Temperature Increase. Genetics
658 *214*, 927-939.
659 25. Hong, Y., Roy, R., and Ambros, V. (1998). Developmental regulation of a cyclin-
660 dependent kinase inhibitor controls postembryonic cell cycle progression in Caenorhabditis
661 elegans. Development *125*, 3585-3597.
662 26. Hsu, C.H., Altschuler, S.J., and Wu, L.F. (2019). Patterns of Early p21 Dynamics
663 Determine Proliferation-Senescence Cell Fate after Chemotherapy. Cell *178*, 361-373 e312.
664 27. Hur, W., Kemp, J.P., Jr., Tarzia, M., Deneke, V.E., Marzluff, W.F., Duronio, R.J., and Di
665 Talia, S. (2020). CDK-Regulated Phase Separation Seeded by Histone Genes Ensures Precise
666 Growth and Function of Histone Locus Bodies. Dev Cell.
667 28. Jones, S.M., and Kazlauskas, A. (2001). Growth-factor-dependent mitogenesis requires
668 two distinct phases of signalling. Nat Cell Biol *3*, 165-172.
669 29. Katsanos, D., Koneru, S.L., Mestek Boukhibar, L., Gritti, N., Ghose, R., Appleford, P.J.,
670 Doitsidou, M., Woollard, A., van Zon, J.S., Poole, R.J.*, et al.* (2017). Stochastic loss and gain of
671 symmetric divisions in the C. elegans epidermis perturbs robustness of stem cell number. PLoS
672 Biol *15*, e2002429.
673 30. Katz, W.S., Hill, R.J., Clandinin, T.R., and Sternberg, P.W. (1995). Different levels of the
674 C. elegans growth factor LIN-3 promote distinct vulval precursor fates. Cell *82*, 297-307.
675 31. Kocsisova, Z., Kornfeld, K., and Schedl, T. (2018). Cell cycle accumulation of the
676 proliferating cell nuclear antigen PCN-1 transitions from continuous in the adult germline to
677 intermittent in the early embryo of C. elegans. BMC Dev Biol *18*, 12.
678 32. Kohrman, A.Q., and Matus, D.Q. (2017). Divide or Conquer: Cell Cycle Regulation of
679 Invasive Behavior. Trends Cell Biol *27*, 12-25.
680 33. Leise, W.F., 3rd, and Mueller, P.R. (2004). Inhibition of the cell cycle is required for
681 convergent extension of the paraxial mesoderm during Xenopus neurulation. Development *131*,
682 1703-1715.
683 34. Leung, B., Hermann, G.J., and Priess, J.R. (1999). Organogenesis of the Caenorhabditis
684 elegans intestine. Dev Biol *216*, 114-134.
685 35. Martin, B.L. (2016). Factors that coordinate mesoderm specification from
686 neuromesodermal progenitors with segmentation during vertebrate axial extension. Semin Cell
687 Dev Biol *49*, 59-67.
688 36. Matus, D.Q., Chang, E., Makohon-Moore, S.C., Hagedorn, M.A., Chi, Q.Y., and
689 Sherwood, D.R. (2014). Cell division and targeted cell cycle arrest opens and stabilizes
690 basement membrane gaps. Nature communications *5*, 13.
691 37. Matus, D.Q., Lohmer, L.L., Kelley, L.C., Schindler, A.J., Kohrman, A.Q., Barkoulas, M.,
692 Zhang, W., Chi, Q., and Sherwood, D.R. (2015). Invasive Cell Fate Requires G1 Cell-Cycle

Arrest and Histone Deacetylase-Mediated Changes in Gene Expression. Developmental Cell *35*, 162-174.
38. Medwig-Kinney, T.N., Smith, J.J., Palmisano, N.J., Tank, S., Zhang, W., and Matus, D.Q. (2020). A developmental gene regulatory network for C. elegans anchor cell invasion. Development *147*.
39. Miller, I., Min, M., Yang, C., Tian, C., Gookin, S., Carter, D., and Spencer, S.L. (2018). Ki67 is a Graded Rather than a Binary Marker of Proliferation versus Quiescence. Cell Rep *24*, 1105-1112 e1105.
40. Min, M., Rong, Y., Tian, C., and Spencer, S. (2020). Temporal integration of mitogen history in mother cells controls proliferation of daughter cells. Science.
41. Moser, J., Miller, I., Carter, D., and Spencer, S.L. (2018). Control of the Restriction Point by Rb and p21. Proc Natl Acad Sci U S A *115*, E8219-E8227.
42. Murakami, M.S., Moody, S.A., Daar, I.O., and Morrison, D.K. (2004). Morphogenesis during Xenopus gastrulation requires Wee1-mediated inhibition of cell proliferation. Development *131*, 571-580.
43. Newport, J., and Kirschner, M. (1982). A major developmental transition in early Xenopus embryos: I. characterization and timing of cellular changes at the midblastula stage. Cell *30*, 675-686.
44. Oki, T., Nishimura, K., Kitaura, J., Togami, K., Maehara, A., Izawa, K., Sakaue-Sawano, A., Niida, A., Miyano, S., Aburatani, H.*, et al.* (2014). A novel cell-cycle-indicator, mVenus-p27K-, identifies quiescent cells and visualizes G0-G1 transition. Sci Rep *4*, 4012.
45. Osborn, D.P., Li, K., Hinits, Y., and Hughes, S.M. (2011). Cdkn1c drives muscle differentiation through a positive feedback loop with Myod. Dev Biol *350*, 464-475.
46. Overton, K.W., Spencer, S.L., Noderer, W.L., Meyer, T., and Wang, C.L. (2014). Basal p21 controls population heterogeneity in cycling and quiescent cell cycle states. Proc Natl Acad Sci U S A *111*, E4386-4393.
47. Ozpolat, B.D., Handberg-Thorsager, M., Vervoort, M., and Balavoine, G. (2017). Cell lineage and cell cycling analyses of the 4d micromere using live imaging in the marine annelid Platynereis dumerilii. Elife *6*.
48. Pardee, A.B. (1974). A restriction point for control of normal animal cell proliferation. Proc Natl Acad Sci U S A *71*, 1286-1290.
49. Rasmussen, J.P., Feldman, J.L., Reddy, S.S., and Priess, J.R. (2013). Cell interactions and patterned intercalations shape and link epithelial tubes in C. elegans. PLoS Genet *9*, e1003772.
50. Ruijtenberg, S., and van den Heuvel, S. (2015). G1/S Inhibitors and the SWI/SNF Complex Control Cell-Cycle Exit during Muscle Differentiation. Cell.
51. Sakaue-Sawano, A., Kurokawa, H., Morimura, T., Hanyu, A., Hama, H., Osawa, H., Kashiwagi, S., Fukami, K., Miyata, T., Miyoshi, H.*, et al.* (2008). Visualizing Spatiotemporal Dynamics of Multicellular Cell-Cycle Progression. Cell *132*, 487-498.
52. Schwarz, C., Johnson, A., Koivomagi, M., Zatulovskiy, E., Kravitz, C.J., Doncic, A., and Skotheim, J.M. (2018). A Precise Cdk Activity Threshold Determines Passage through the Restriction Point. Molecular cell *69*, 253-264 e255.
53. Shoji, W., Yee, C.S., and Kuwada, J.Y. (1998). Zebrafish semaphorin Z1a collapses specific growth cones and alters their pathway in vivo. Development *125*, 1275-1283.
54. Spencer, S.L., Cappell, S.D., Tsai, F.C., Overton, K.W., Wang, C.L., and Meyer, T. (2013). The proliferation-quiescence decision is controlled by a bifurcation in CDK2 activity at mitotic exit. Cell *155*, 369-383.
55. Sternberg, P.W. (1984). Control of cell lineage during nematode development (Cambridge, MA: Massachusetts Institute of Technology).
56. Sternberg, P.W., and Horvitz, H.R. (1986). Pattern formation during vulval development in C. elegans. Cell *44*, 761-772.

57. Strzyz, P.J., Lee, H.O., Sidhaye, J., Weber, I.P., Leung, L.C., and Norden, C. (2015). Interkinetic nuclear migration is centrosome independent and ensures apical cell division to maintain tissue integrity. Dev Cell *32*, 203-219.
58. Sugiyama, M., Saitou, T., Kurokawa, H., Sakaue-Sawano, A., Imamura, T., Miyawaki, A., and Iimura, T. (2014). Live imaging-based model selection reveals periodic regulation of the stochastic G1/S phase transition in vertebrate axial development. PLoS Comput Biol *10*, e1003957.
59. Sugiyama, M., Sakaue-Sawano, A., Iimura, T., Fukami, K., Kitaguchi, T., Kawakami, K., Okamoto, H., Higashijima, S., and Miyawaki, A. (2009). Illuminating cell-cycle progression in the developing zebrafish embryo. Proc Natl Acad Sci U S A *106*, 20812-20817.
60. Sulston, J.E., and Horvitz, H.R. (1977). Post-embryonic cell lineages of the nematode, Caenorhabditis elegans. Dev Biol *56*, 110-156.
61. Sun, D., and Buttitta, L. (2017). States of G0 and the proliferation-quiescence decision in cells, tissues and during development. Int J Dev Biol *61*, 357-366.
62. Tomura, M., Sakaue-Sawano, A., Mori, Y., Takase-Utsugi, M., Hata, A., Ohtawa, K., Kanagawa, O., and Miyawaki, A. (2013). Contrasting quiescent G0 phase with mitotic cell cycling in the mouse immune system. PLoS One *8*, e73801.
63. van der Horst, S.E.M., Cravo, J., Woollard, A., Teapal, J., and van den Heuvel, S. (2019). C. elegans Runx/CBFbeta suppresses POP-1 TCF to convert asymmetric to proliferative division of stem cell-like seam cells. Development *146*.
64. van Rijnberk, L.M., van der Horst, S.E., van den Heuvel, S., and Ruijtenberg, S. (2017). A dual transcriptional reporter and CDK-activity sensor marks cell cycle entry and progression in C. elegans. PLoS One *12*, e0171600.
65. Yang, H.W., Chung, M., Kudo, T., and Meyer, T. (2017). Competing memories of mitogen and p53 signalling control cell-cycle entry. Nature *549*, 404-408.
66. Yang, R., and Feldman, J.L. (2015). SPD-2/CEP192 and CDK Are Limiting for Microtubule-Organizing Center Function at the Centrosome. Curr Biol *25*, 1924-1931.
67. Yang, Z.J., Broz, D.K., Noderer, W.L., Ferreira, J.P., Overton, K.W., Spencer, S.L., Meyer, T., Tapscott, S.J., Attardi, L.D., and Wang, C.L. (2015). p53 suppresses muscle differentiation at the myogenin step in response to genotoxic stress. Cell Death Differ *22*, 560-573.
68. Zerjatke, T., Gak, I.A., Kirova, D., Fuhrmann, M., Daniel, K., Gonciarz, M., Muller, D., Glauche, I., and Mansfeld, J. (2017). Quantitative Cell Cycle Analysis Based on an Endogenous All-in-One Reporter for Cell Tracking and Classification. Cell Rep *19*, 1953-1966.
69. Zetterberg, A., and Larsson, O. (1985). Kinetic analysis of regulatory events in G1 leading to proliferation or quiescence of Swiss 3T3 cells. Proc Natl Acad Sci U S A *82*, 5365-5369.
70. Ziel, J.W., Hagedorn, E.J., Audhya, A., and Sherwood, D.R. (2009). UNC-6 (netrin) orients the invasive membrane of the anchor cell in C. elegans. Nature Cell Biology *11*, 183-189.
71. Zielke, N., and Edgar, B.A. (2015). FUCCI sensors: powerful new tools for analysis of cell proliferation. Wiley Interdiscip Rev Dev Biol *4*, 469-487.
72. Zwang, Y., Sas-Chen, A., Drier, Y., Shay, T., Avraham, R., Lauriola, M., Shema, E., Lidor-Nili, E., Jacob-Hirsch, J., Amariglio, N.*, et al.* (2011). Two phases of mitogenic signaling unveil roles for p53 and EGR1 in elimination of inconsistent growth signals. Molecular cell *42*, 524-535.

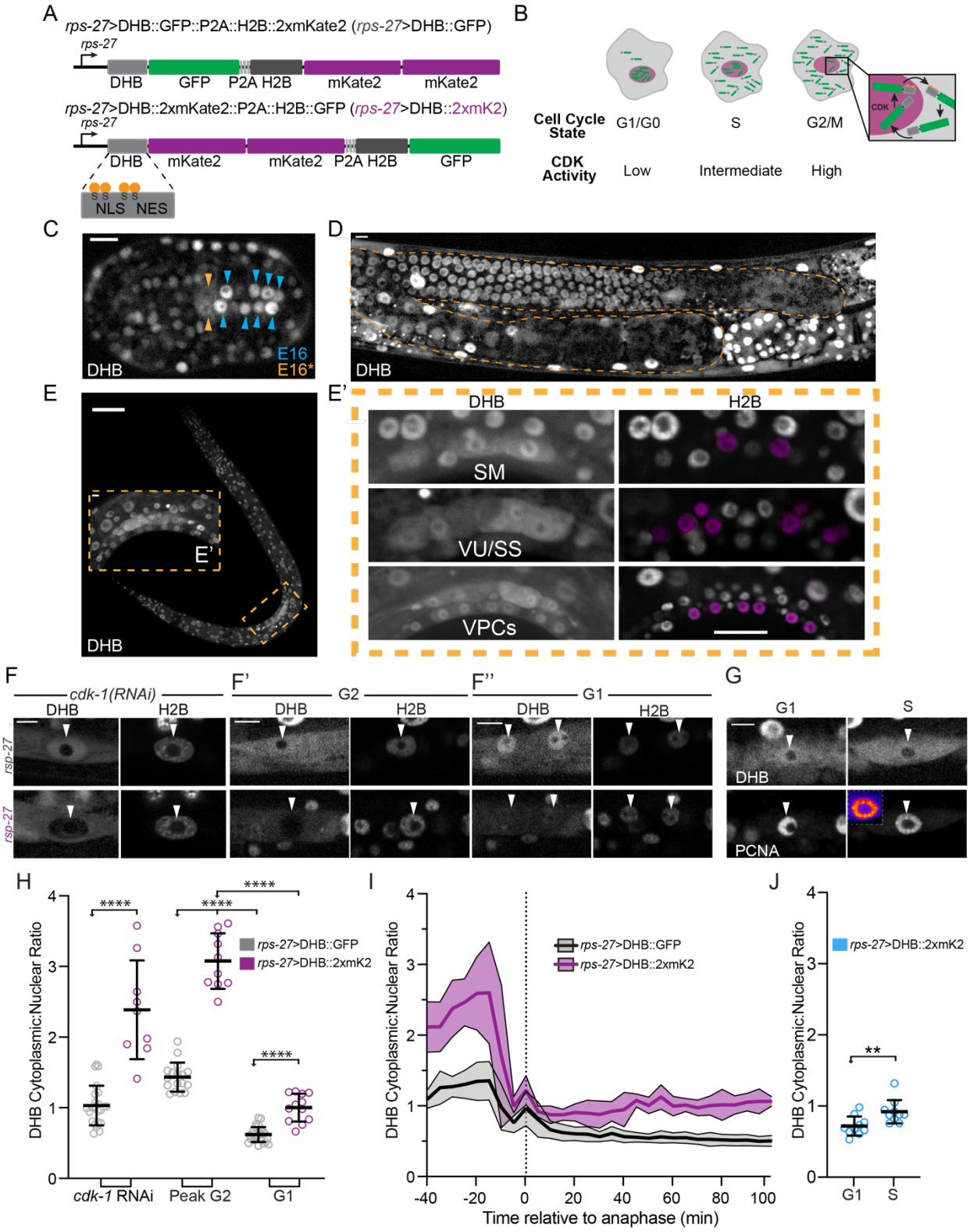
A
rps-27>DHB::GFP::P2A::H2B::2xmKate2 (rps-27>DHB::GFP)
rps-27
DHB
GFP
P2A H2B
mKate2
mKate2
rps-27>DHB::2xmKate2::P2A::H2B::GFP (rps-27>DHB::2xmK2)
rps-27
DHB
mKate2
mKate2
P2A H2B
GFP
NLS
NES
B
Cell Cycle State
G1/G0
S
G2/M
CDK
CDK Activity
Low
Intermediate
High
C
DHB
E16
E16*
D
DHB
E
E'
DHB
E'
DHB
H2B
SM
VU/SS
VPCs
F
cdk-1(RNAi)
DHB
H2B
F'
G2
DHB
H2B
F''
G1
DHB
H2B
rsp-27
rsp-27
G
G1
S
DHB
PCNA
H
DHB Cytoplasmic:Nuclear Ratio
****
****
****
****
rps-27>DHB::GFP
rps-27>DHB::2xmK2
cdk-1 RNAi
Peak G2
G1
I
DHB Cytoplasmic:Nuclear Ratio
rps-27>DHB::GFP
rps-27>DHB::2xmK2
Time relative to anaphase (min)
J
DHB Cytoplasmic:Nuclear Ratio
rps-27>DHB::2xmK2
**
G1
S

Figure 1. Generation of a CDK sensor for live cell cycle visualization in *C. elegans*. (A) Schematic of CDK sensor fused to GFP (top) or two copies of mKate2 (bottom) and a nuclear mask (H2B::FP) separated by a self-cleaving peptide (P2A). Inset: nuclear-localization signal (NLS), nuclear export signal (NES), CDK consensus phosphorylation sites on serine (S). (B) Schematic of CDK sensor translocation during the cell cycle. (C) Quiescent E16 cells (blue arrows) versus the cycling E16* star cells (orange) arrows. (D-E) Confocal micrograph montage of CDK sensor in the *C. elegans* germline (D, orange dashed line) and L3 stage larvae (E). Three somatic tissues are highlighted (inset, dashed orange box) shown at higher magnification in E', with pseudo colored nuclei (magenta) depicting cells of interest. (F, G) Representative images of sensor expression in SM cells following *cdk-1* RNAi treatment; at peak G2 (F') and 20 minutes after anaphase during G1 (F'') in DHB::GFP (grey) and DHB::2xmKate2 (magenta) and DHB::2xmKate2 co-expressed with PCNA (*pcn-1*>PCN-1::GFP), inset highlights PCNA puncta in S phase. (H) Dot plot depicting dynamic ranges of the two CDK sensor variants, measured by the cytoplasmic:nuclear ratio of DHB mean fluorescent intensity, at the peak of G_2 and G_1 in the SMs ($n \geq 9$). (I) Plot of DHB cytoplasmic:nuclear ratio in SM cells during one round of cell division, measured every 5 minutes ($n=4$ per strain). Dotted line indicates time of anaphase. Error bars and shaded error bands depict mean±standard deviation. (J) Dot plot depicting range of G1 and S phase in DHB::2xmKate2 based on PCNA localization ($n \geq 7$ per strain). ** $p \leq 0.01$, ****$p \leq 0.0001$ Significance as determined by statistical simulation; exact *p*-values in **Table S1**. Scale bar = 10 µm except in (E; 20 µm and F; 5 µm).

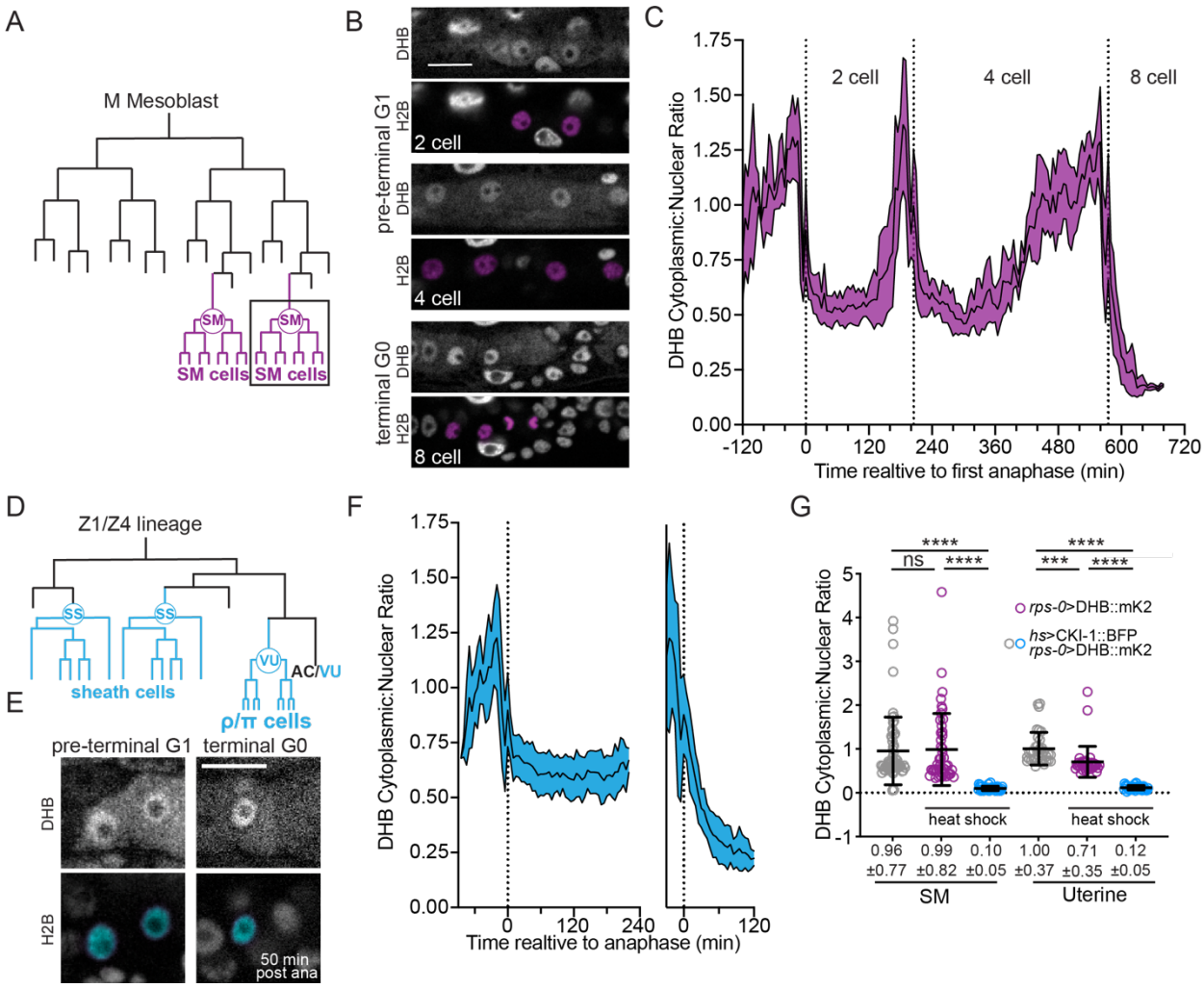

Figure 2. Sex myoblasts and somatic gonad cells exit terminal divisions into a CDK^{low} state. SM (A) and uterine (D) lineage schematics. (B) Micrographs of a time-lapse movie showing SM cells (B) and uterine cells (E) at G_1 in pre-terminal divisions and G_0 upon terminal differentiation. Quantification of CDK sensor in SM cells (C; $n \geq 10$) and uterine cells (F; $n \geq 13$). (G) Quantification of CDK sensor localization in SM cells and uterine cells following ectopic expression of CKI-1 (*hsp*>CKI-1::2xmTagBFP2) compared to non-heat shock controls and heat shock animals without the inducible transgene ($n \geq 36$ per treatment). Scale bars = 10 µm. Pseudo colored nuclei (magenta, B; cyan, E) indicate cells of interest. Dotted line indicates time of anaphase. Line and shaded error bands depict mean ± standard deviation, time series measured every 5 minutes. ****$p \leq 0.0001$ Significance as determined by statistical simulations; *p*-values in **Table S1**.

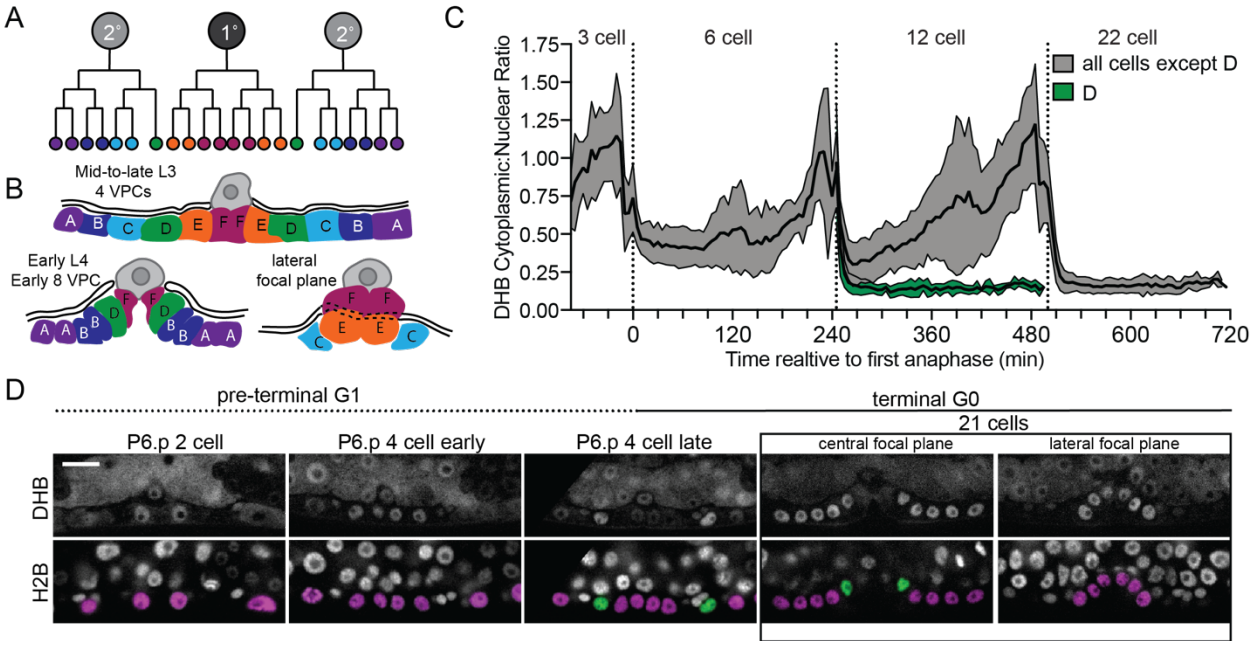

Figure 3. Vulval precursor cells exit terminal divisions into a CDK^{low} state. (A) Schematic of primary (1°) and secondary (2°) fated vulval precursor cells (VPCs). (B) All of the VPCs, with the exception of the D cells, divide to facilitate vulval morphogenesis. (C) Time series of CDK sensor localization in the 1° and 2° VPCs, as measured every 5 min. Note that the terminally differentiated D cells are born into a CDK^{low} state ($n \geq 9$). Dotted line indicates time of anaphase. Shaded error bands depict mean±standard deviation. (D) Representative images of CDK sensor localization in the VPCs from the P6.p 2-cell stage to 8-cell stage. Nuclei (H2B) are highlighted in magenta for non-D cell 1° and 2° VPCs and green for the D cells. Scale bar = 10 µm.

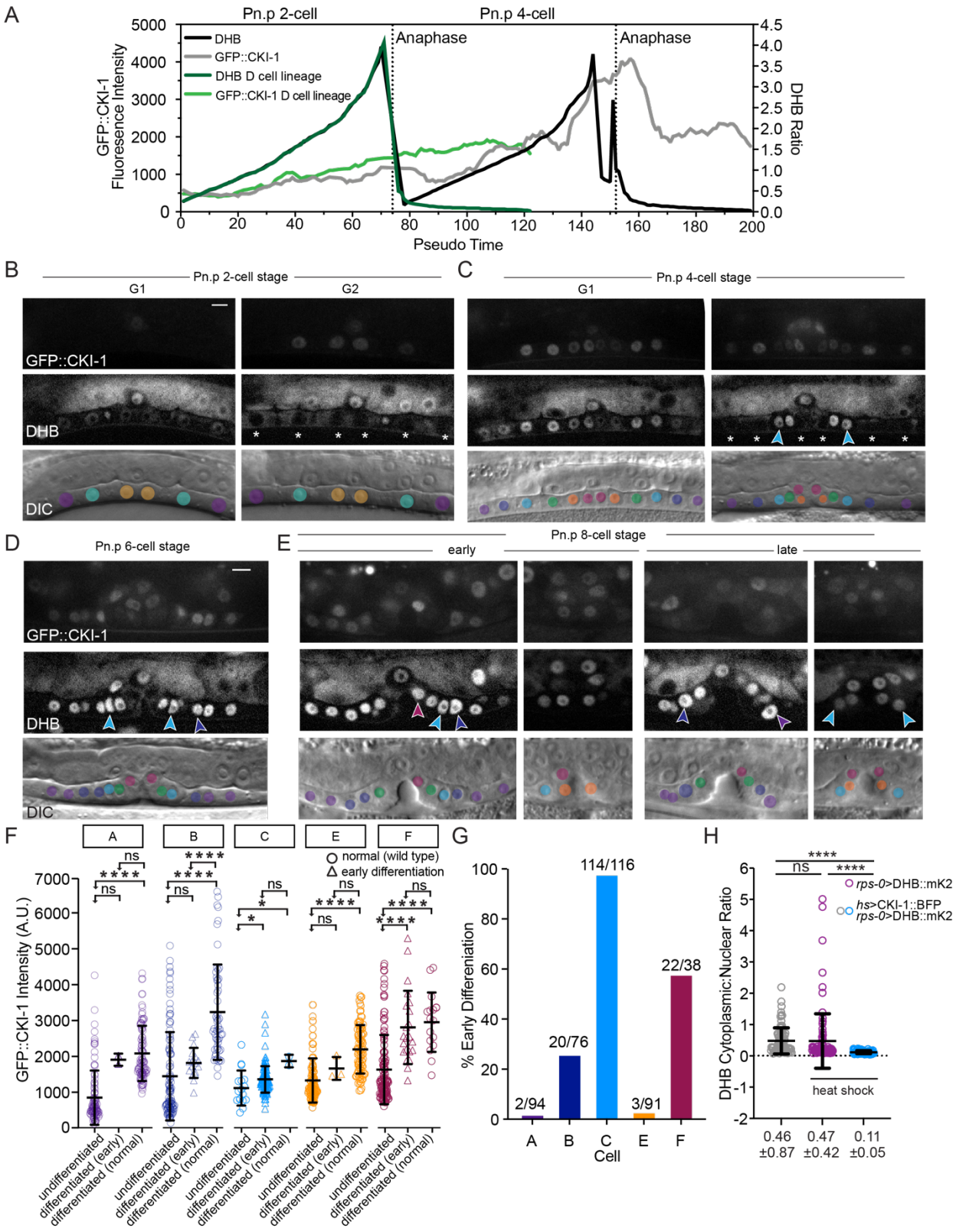
A
Pn.p 2-cell
Pn.p 4-cell
Anaphase
Anaphase
DHB
GFP::CKI-1
DHB D cell lineage
GFP::CKI-1 D cell lineage
GFP::CKI-1 Fluoresence Intensity
DHB Ratio
Pseudo Time
B
Pn.p 2-cell stage
G1
G2
C
Pn.p 4-cell stage
G1
GFP::CKI-1
DHB
DIC
D
Pn.p 6-cell stage
E
Pn.p 8-cell stage
early
late
F
normal (wild type)
early differentiation
GFP::CKI-1 Intensity (A.U.)
undifferentiated
differentiated (early)
differentiated (normal)
G
% Early Differeniation
114/116
20/76
22/38
2/94
3/91
Cell
H
DHB Cytoplasmic:Nuclear Ratio
rps-0>DHB::mK2
hs>CKI-1::BFP
rps-0>DHB::mK2
heat shock
0.46 ±0.87
0.47 ±0.42
0.11 ±0.05

850
851
852

853 **Figure 4. CKI-1 levels peak prior to terminal differentiation.** (A) CDK sensor activity and CKI-
854 1 levels across pseudo-time, DHB ratios for all VPCs (black line) and D cells (dark green line).
855 GFP::CKI-1 fluorescence intensity in VPCs (grey line) and D cell (light green line). (B)
856 Representative images of VPCs at the Pn.p 2-cell stage at G_1 and G_2 (white asterisk). (C)
857 Representative images of VPCs at the Pn.p 4-cell stage at G_1 and G_2; early differentiated C cells
858 (cyan arrows) with low levels of GFP::CKI-1. (D-E) Representative images of VPCs at the Pn.p
859 6-cell stage (D) and 8-cell stage (E); arrows show early differentiated C (cyan) and B cell (dark
860 blue), F cell (magenta arrow), and A cell (purple arrow). (F) GFP::CKI-1 fluorescence intensity in
861 each cell of the VPC lineage. (G) Percentage of cells of each lineage that showed early
862 differentiation and did not undergo their final division. (H) Overexpression of CKI-1 via heat shock
863 causes pre-terminally differentiated cells to enter G_0 state. Scale bar = 10 μm. *$p \leq 0.05$,
864 ****$p \leq 0.0001$ Significance as determined by statistical simulations; *p*-values in **Table S1**.
865

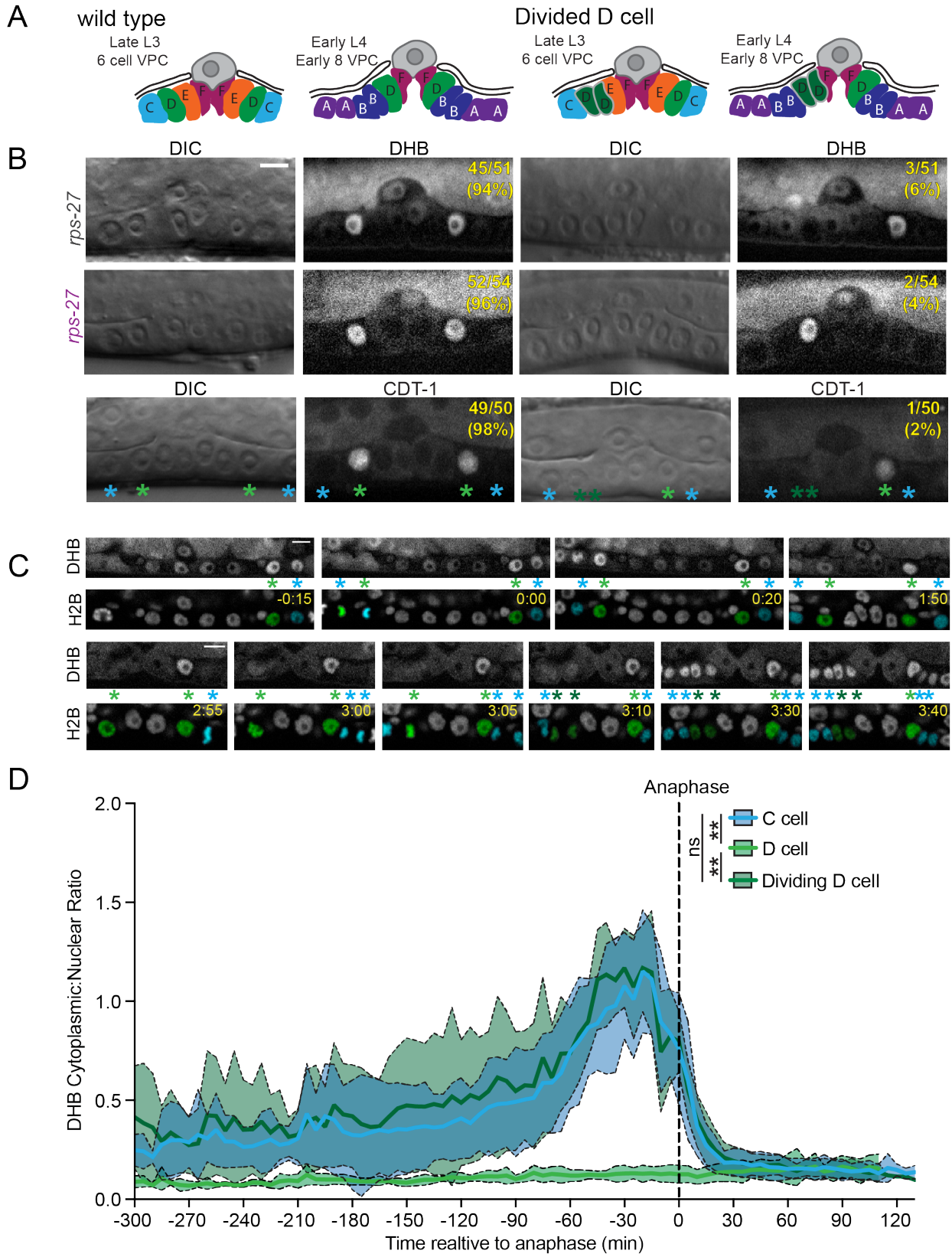
A
wild type
Late L3
6 cell VPC
Early L4
Early 8 VPC
Divided D cell
Late L3
6 cell VPC
Early L4
Early 8 VPC
B
DIC
DHB
DIC
DHB
rps-27
45/51
(94%)
3/51
(6%)
rps-27
52/54
(96%)
2/54
(4%)
DIC
CDT-1
DIC
CDT-1
49/50
(98%)
1/50
(2%)
C
DHB
H2B
-0:15
0:00
0:20
1:50
DHB
H2B
2:55
3:00
3:05
3:10
3:30
3:40
D
Anaphase
C cell
D cell
Dividing D cell
ns
**
**
DHB Cytoplasmic:Nuclear Ratio
2.0
1.5
1.0
0.5
0.0
-300
-270
-240
-210
-180
-150
-120
-90
-60
-30
0
30
60
90
120
Time realtive to anaphase (min)

868 **Figure 5. CDK activity predicts a cryptic stochastic fate decision in an invariant cell lineage.**
869 (A) Schematic of wild type vulva and vulva with a divided D cell. (B) Representative images at the
870 Pn.p 6 cell stage from CDK sensor strains (top, middle) and endogenous *cdt-1::GFP* (bottom),
871 showing wild type vulva on the left and vulva with a divided D cell on the right. Penetrance of each
872 phenotype for each strain is annotated on the DHB image. (C) Frames from a time-lapse with a
873 dividing D cell (left) (see Movie S5). Nuclei (H2B) are highlighted in green for the D cell and cyan
874 for the C cells. (D) DHB ratio for C cell, terminally differentiated D cell and dividing D cell. Dotted
875 line indicates time of anaphase. Line and shaded error bands depict mean±standard deviation.
876 Green asterisks or pseudo colored nuclei mark the D cell and cyan asterisks or pseudo colored
877 nuclei mark the C cell, scale bar = 10 μm. ** $p \leq 0.01$, *P* values determined Significance as
878 determined by statistical simulations; *p*-values in **Table S1**.
879

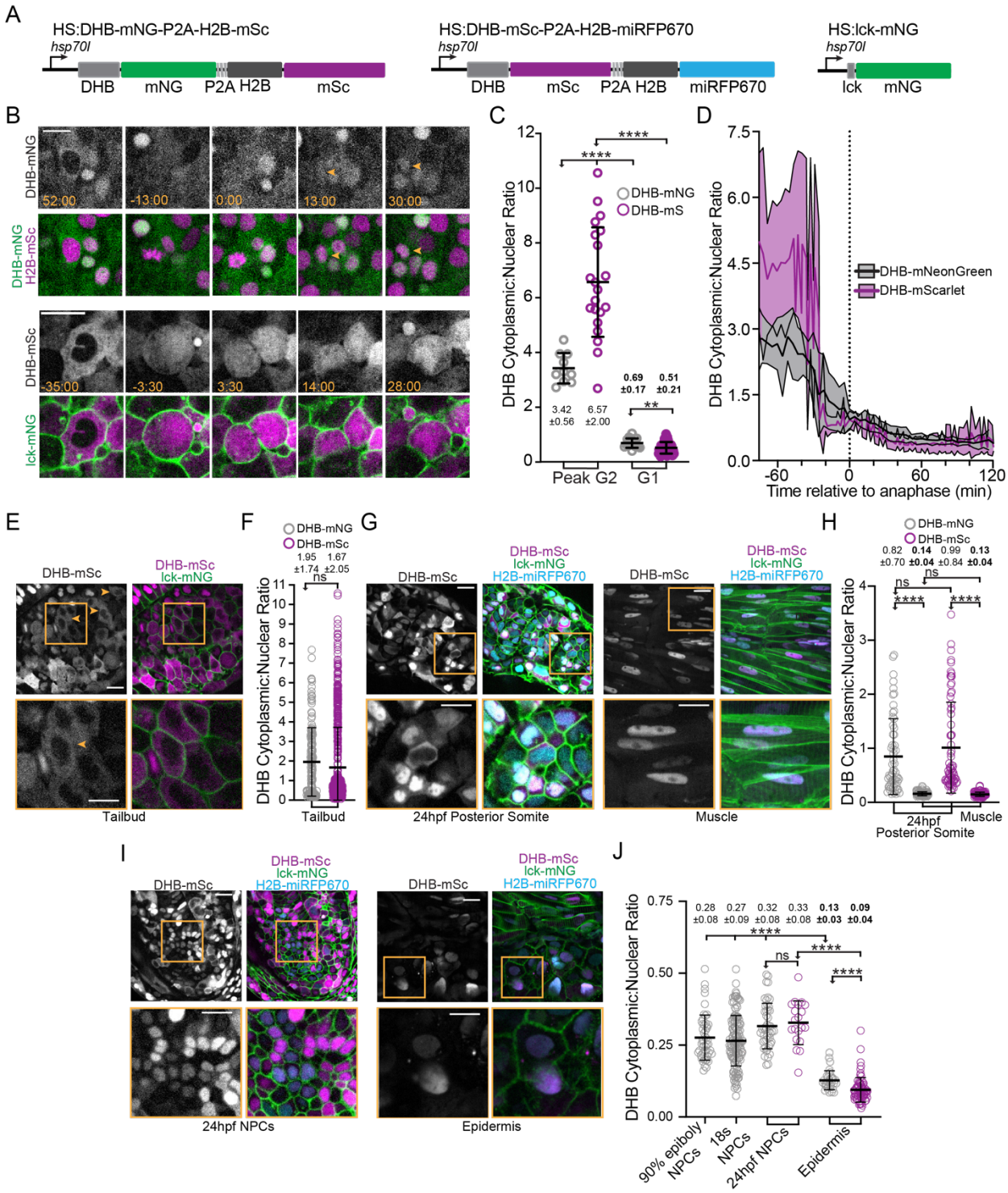

Figure 6. Generation of inducible CDK sensor transgenic lines in the zebrafish. (A) Schematics of inducible zebrafish variants of the CDK sensor fused to mNG (left) or mSc (middle) and a nuclear mask (H2B::FP) separated by a self-cleaving peptide (P2A). Schematic of inducible membrane marker (lck-mNG; right). (B-D) Frames (B), dot plot (C) and DHB ratio plot (D) from time lapse of DHB-mNG (top, gray) and DHB-mSc (bottom, magenta) of peak G_2 through anaphase and G_1 (n>10 examined for each). Dotted line indicates time of anaphase. (E-F)

887 Representative micrographs of CDK sensor (E, orange arrows and box inset highlights cytosolic
888 CDK sensor localization) and quantification of DHB ratio (F) in the tailbud. (G-J) Representative
889 micrographs (G, I) and quantification of DHB ratios (H, J) in cells of 24 hpf posterior somites and
890 terminally differentiated muscle at 72 hpf (G), notochord progenitors (NPCs) and epidermis at 72
891 hpf (I). Insets, orange box, Scale bar = 20 μm. Line and error bars depict mean±standard
892 deviation, numbers in **bold** are tissues in G_0. ** $p \leq 0.01$, ****$p \leq 0.0001$ *P* values determined by
893 statistical simulations, exact values reported in **Table S1**.
894
895

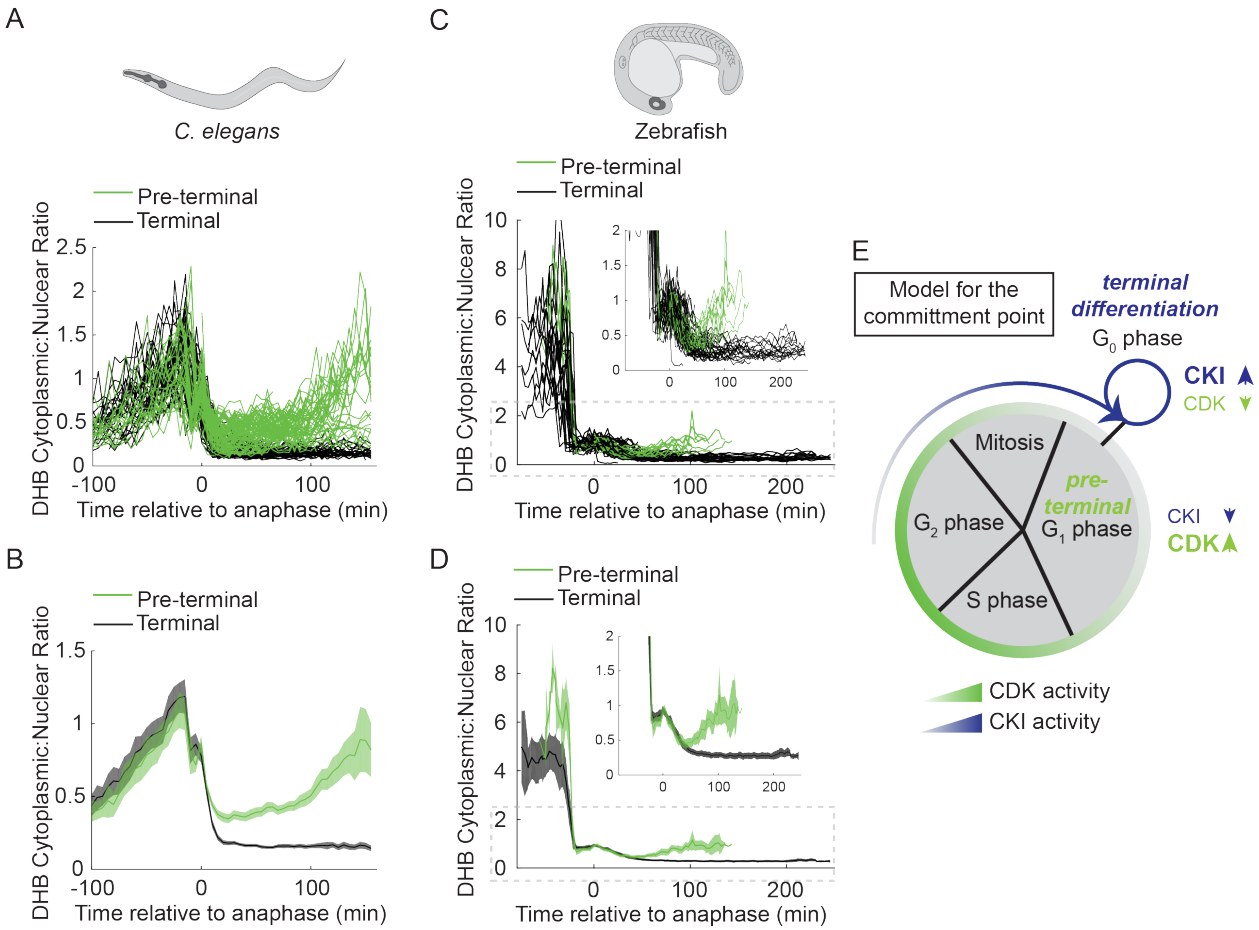

Figure 7. A bifurcation in CDK activity at mitotic exit controls the proliferation-differentiation decision. (A-D) Single-cell traces of CDK activity for all quantified *C. elegans* (A-B) and zebrafish (C-D) cell births for CDK^{inc} cells (green) and CDK^{low} cells (black). DHB ratio of single-cell data (A, C) and mean±95% confidence interval (B, D) are plotted for each cell analyzed relative to anaphase. (E) A model for the metazoan commitment point argues that the G_1/G_0 decision is influenced by a maternal input of CKI activity and that CDK activity shortly after mitotic exit determines future cell fate.